geoconvention
Calgary • Canada • May 7-11 2018

Source Mechanisms of Hydraulic-Fracturing Induced Event Sequences in the Fox Creek Area

Hongliang Zhang, and David W. Eaton
Department of Geoscience, University of Calgary

Summary

Shallow borehole microseismic monitoring was undertaken during a set of multi-stage hydraulic fracturing operation in the Tony Creek dual Microseismic Experiment (ToC2ME). P-wave polarity-based focal-mechanism inversion and 3C P-wave amplitude-based moment-tensor inversion were applied to 17 events induced by hydraulic fracturing treatment. By analyzing the inverted source mechanisms, the 17 induced events could be classified into two groups: group one, N-S or E-W trending strike-slip; group two, NE-SW trending strike-slip with low dip angle or NW-SE dip-slip with high dip angle. For the events within group one, the source mechanisms are dominated by DC (>75%) accompanied by minor non- DC components. For the events in group two, the source mechanisms exhibit significant non-DC components, consistent with minor tensile opening/closing, or complex fault geometry. The latter might include multiple intersecting fractures, dilatant jogs created at the overlapping areas of multiple fractures, or non-planar fault geometry.

Introduction

In this study, we undertake a detailed investigation of 17 earthquakes with magnitudes > M1.5 that occurred between November 10 and November 29, 2016. All of the events occurred during a multiwell hydraulic-fracturing completions program west of Fox Creek, Alberta. This study extends previous induced-seismicity investigations in this area through the use of a dense shallow well array to investigate an extended sequence of events. We begin by introducing the dataset and then we outline our focal-mechanism inversion and moment-tensor inversion approaches. Finally, comparisons between inverted focalmechanisms and moment-tensor solutions are made to provide insights into the geomechanical significance of the events.

Methods

The focal mechanism solutions were obtained in this study to estimate source mechanisms using the polarities of observed P-wave first motions. The polarities were picked on the vertical component, which usually has the highest-amplitude response for P-wave arrivals compared with the horizontal components. The focal mechanism can then be estimated using a grid search method that minimizes the misfit between predicted and observed polarities. During this process, all possible strike, dip, rake values were considered with a sampling of 2° for each.

We performed the moment-tensor inversion based on the 3C amplitudes of direct P-wave in a 1-D layered isotropic medium. For a homogeneous region around a source located at the origin, the ith component of particle motion arising from the radiated P-wave can be represented as (Aki and Richards, 2002):

$$u_i^P(x,t) = (4\pi r \rho \alpha^3)^{-1}\{r_i r_j r_k M_{jk}\} \cdot \omega(t-\tau_P)\,, \quad (1)$$

where r denotes the source-receiver distance; ρ and α are density and P-wave velocity; i is the direction cosine at the source of the ray to the receiver; $\omega(t)$ is the displacement time function at the source, τ_P is the traveltime from source to receiver, and the dot notion denotes time derivative. Terms within the curly braces represent the P-wave radiation pattern, and the summation convention is used in this equation. In addition, for a 1-D layered velocity model, ρ represents the average density, while r and

α denote the distance and average P-wave velocity along the raypath, respectively. These parameters can be obtained through raytracing.

Based on equation (1), the observed 3C ground displacement amplitudes of direction P-wave can be cast in matrix notation as

$$\mathbf{d}^{obs} = \mathbf{Gm} + \mathbf{n}, \tag{2}$$

The least-squares solution to this overdetermined problem is given by:

$$\hat{\mathbf{m}} = (\mathbf{G}^T\mathbf{G})^{-1}\mathbf{G}^T\mathbf{d}^{obs}, \tag{3}$$

Dataset

The study area as shown in Figure 1 is situated west of Fox Creek, Alberta. Microseismic monitoring was used to record continuous ground-motion data between October 25 and November 29, 2016 over a four-well hydraulic fracturing treatment. The recording system consists of 1 accelerometer, 6 broadband seismometers and an array of 69 shallow borehole geophone system and two surface three-component geophones. In terms of the shallow borehole systems, each has three one component geophones and one three-component geophone. In this study, only the 69 three-component geophones (marked in blue triangle in Figure 1) were used. This distribution of stations provides good azimuthal coverage for the moment tensor calculations. As marked in red circles in Figure 1, 17 induced events with magnitude larger than M 1.5 were observed during the monitoring period. Table 1 shows the origin times and event magnitudes reported on a regional event catalog.

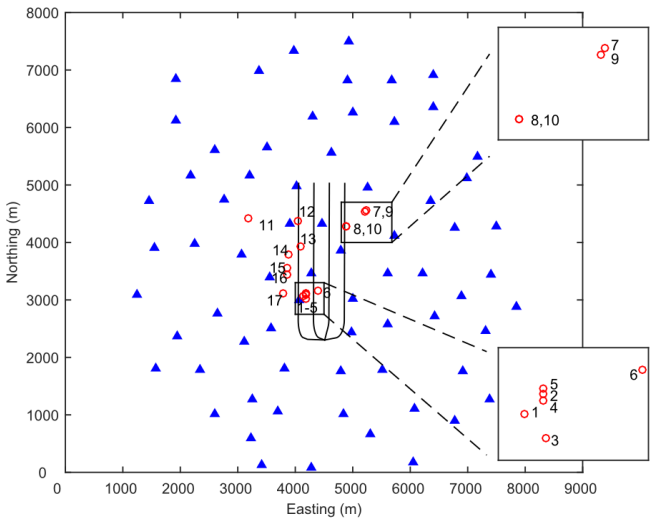

Figure 1 Map view of locations of horizontal wells (black lines), shallow borehole geophones (blue triangles) and 17 induced events (red open circles) used in this study.

Table 1 Catalog of 17 induced events reported on a regional monitoring network.

Event ID	Date and Time (UTC)	Reported Magnitude
1	2016/11/10 03:05:55	M_W 3.1
2	2016/11/10 09:55:29	M_W 2.8
3	2016/11/11 02:33:46	M_W 2.6
4	2016/11/11 11:24:09	M_W 2.8
5	2016/11/15 13:28:11	MI 1.59
6	2016/11/21 21:39:45	MI 1.84
7	2016/11/22 10:04:31	MI 2.1
8	2016/11/22 11:21:06	MI 1.5
9	2016/11/22 13:18:44	MI 1.68
10	2016/11/22 18:18:25	M_W 2.6
11	2016/11/25 05:31:25	M_W 3.4
12	2016/11/25 21:24:01	M_W 3.5
13	2016/11/27 14:52:51	M_W 2.8
14	2016/11/28 06:53:38	M_W 3
15	2016/11/28 15:35:27	MI 1.86
16	2016/11/29 04:12:48	M_W 3
17	2016/11/29 10:15:25	M_W 3.6

Results

Before performing the moment-tensor inversion, the raw waveform data need to be pre-processed, which includes instrument-response removal, conversion from ground velocity to displacement, applying a rotation to correct for geophone orientation, DC-component removal and bandpass filtering. The geophone orientations were determined by hodogram analysis of waveforms generated by hammer blows at specified azimuths (north and east) around each borehole.

Table 2 summarizes the focal-mechanism-inversion results based on P-wave polarities as well as the moment-tensor-inversion results based on 3C displacement amplitudes of direct P-wave. For some events, a set of focal mechanism solutions were obtained that fit the observed polarities equally well. In general, however, there are two dominant focal mechanisms within the 17 induced events. Events 1-6 and 11-17 share a similar strike-slip focal mechanism with high dip angles typically >85°. The two nodal planes for this group strike N-S and E-W. For events 7-10, the two nodal planes of the focal mechanism exhibit either NS-SW trending strike-dips with dip angles between 50° - 60° or NW-SE trending strike-slips with high dip angles (typically >85°) accompanied by significant thrust-faulting component.

Table 2 Summary of best-fitting focal-mechanism solutions and moment-tensor solutions.

Event ID	Focal Mechanism	Moment Tensor	Event ID	Focal Mechanism	Moment Tensor
1			2		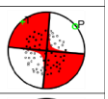
3			4		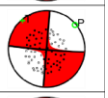
5			6		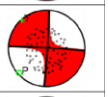
7			8		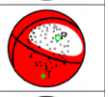
9			10		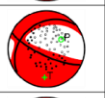
11			12		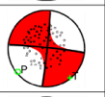
13			14		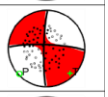
15			16		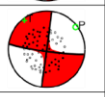
17					

Table 3 Source parameters resulting from the moment-tensor inversion.

Event ID	Moment Magnitude (M_w)	Misfit (%)	Fault Planes for best DC (strike, dip, rake)
1	3.29	11.4	(186, 90, -178) (96, 88, 0)
2	2.77	17.1	(5, 89, 179) (95, 89, 1)
3	2.83	11.3	(185, 89, 177) (275, 87, 1)
4	3.01	10.8	(185, 90, -178) (95, 88, 0)
5	2.48	10.1	(184, 89, 180) (274, 90, 1)
6	2.52	11.1	(4, 88, -179) (273, 89, -2)
7	2.83	12.0	(114, 82, -58) (216, 33, -166)
8	2.47	13.1	(112, 75, -70) (239, 25, -141)
9	2.51	18.1	(98, 80, -53) (202, 38, -163)
10	2.72	12.7	(114, 75, -62) (230, 31, -151)
11	3.67	14.4	(184, 73, 173) (276, 83, 17)
12	3.69	11.3	(6, 88, -178) (276, 88, -2)
13	2.72	22.0	(182, 89, 173) (272, 83, 1)
14	3.07	18.2	(181, 84, 172) (272, 82, 6)
15	2.49	10.4	(184, 88, 180) (274, 90, 2)
16	3.15	17.4	(8, 90, 175) (98, 85, 0)
17	3.69	13.0	(186, 83, 177) (276, 87, 7)

Similarly, the moment-tensor-inversion results show two groups of source mechanisms: group one with events 1-6, 11-17 and group two with events 7-10. For group one, the nodal planes the best-fitting DC mechanism are very close to the previously described focal-mechanism-inversion results of this group. On the other hand, for group two, the nodal planes of the best-fitting DC solutions differ from the focal-mechanism solutions. This difference occurs because the moment-tensor solution has additional degrees of freedom that include non-DC components. Other observations can be used to determine which of the nodal planes is more likely. In Figure 1, events 2-5 occur successively along a N-S trending fault, which is consistent with one of nodal planes in the moment-tensor or focal-mechanism solutions. For events 7-10, the relative locations of these four events agree with the NE-SW trending nodal plane.

Source parameters resulting from the moment-tensor inversion are summarized in Table 3. The seismic moment magnitudes were estimated by fitting Brune model (Brune, 1970; Brune, 1971), resulting in magnitudes ranging between M_W 2.47 and M_W 3.69. The misfits between the observed and theoretical P-wave amplitudes are relatively small, with misfits of <15% for most of events.

Figure 2 shows the percentage of each component after the complete moment-tensor decomposition for each of the 17 events. For events 1-6 and 11-17, the focal mechanism is dominated by the DC (>75%) accompanied by minor CLVD and ISO. However, for events 7-10, significant non-DC components are observed (>25%). The non-DC component can be interpreted in various ways. In the context of hydraulic fracturing, volumetric components of the moment tensor could signify a component of tensile opening. On the other hand, non-DC components can also arise from complex source characteristics such as multiple intersecting fractures, dilatant jogs created at the overlapping areas of multiple fractures, or non-planar fault geometry (Zhang et al., 2016). Moment-tensor inversion results may contain artifacts due to a number of factors, such as the S/N for a given dataset, uncalibrated velocity model, anisotropy of velocity model, source location errors and errors in amplitude picks, and inversion algorithm itself. Future work is needed to determine the possible effects from these sources of artifacts.

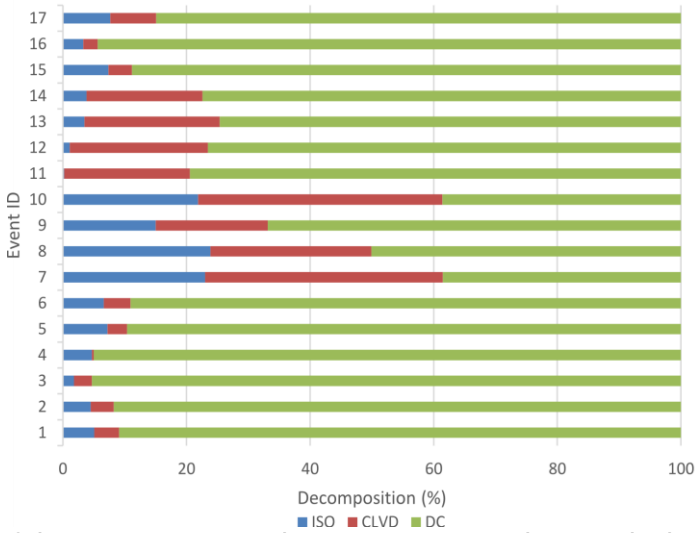

Figure 2 Decomposition of the moment tensor into DC, CLVD and ISO calculated for each event.

Conclusions

The P-wave polarity-based focal-mechanism inversion and P-wave amplitude-based moment-tensor inversion were undertaken for a set of 17 induced events recorded during a hydraulic fracturing program west of Fox Creek, Alberta. In both of the two sets of inversion results, two groups of source mechanisms were identified: group one, predominantly double-couple (DC) N-S or E-W trending strike-slip events; and group two, a set of events exhibiting significant non-DC components with high-dip angle dip-slip (thrust-faulting) or low-dip angle strike-slip. For group one, the nodal planes of the best-fitting DC within the moment tensor are very close to the focal-mechanism-inversion results. For the other group, the nodal plane solutions exhibit slightly larger difference between the two sets of results. In addition, the relative locations of the events within each group can provide aid to choose the real rupture plane from two inverted nodal planes. The full moment tensor were decomposed into three components: ISO, DC and CLVD. The 13 events within group one are dominated by the DC (> 75%) accompanied by minor CLVD and ISO. For the 4 events within group two, significant non-DC were observed (up to > 60%).

Acknowledgements

Two anonymous companies are thanked for providing access to the data of shallow wellbore array. This work was supported by the Natural Sciences and Engineering Research Council of Canada (NSERC) through the NSERC/Chevron Industrial Research Chair in Microseismic System Dynamics and a Collaborative Research and Development (CRD) grant. The CRD grant is also supported by TransAlta Utilities and Nanometrics Ltd. Sponsors of the Microseismic Industry Consortium are also thanked for their ongoing support. Mitacs is thanked for the financial support through Mitacs-Accelerate Graduate Research Internship Program. The event catalog in Table 1 was taken from the TA regional seismic catalog maintained by Nanometrics.

References

Aki, K., and P. G. Richards, 2002, Quantitative Seismology: University Science Books.

Brune, J. N., 1970, Tectonic stress and the spectra of seismic shear waves from earthquakes: Journal of Geophysical Research, 75, 4997-5009.

Brune, J. N., 1971, Correction: Journal of Geophysical Research, 76, 5002.

Zhang, H., D. W. Eaton, G. Li, Y. Liu, and R. M. Harrington, 2016, Discriminating induced seismicity from natural earthquakes using moment tensors and source spectra: Journal of Geophysical Research, 121(2), 972-993.